Geomorphology 389 (2021) 107850

Contents lists available at ScienceDirect

Geomorphology

journal homepage: www.elsevier.com/locate/geomorph

Back analysis of a coastal cliff failure along the Forkastningsfjellet coastline, Svalbard: Implications for controlling and triggering factors

D. Kuhn [a,*], J. Torizin [a], M. Fuchs [a], R.L. Hermanns [b,c], T.F. Redfield [b], D. Balzer [a]

[a] Federal Institute for Geosciences and Natural Resources, Stilleweg 2, 30655 Hannover, Germany
[b] Geological Survey of Norway, Postbox 6315 Torgarden, N–7491 Trondheim, Norway
[c] Department of Geosciences and Petroleum, Norwegian University of Science and Technology, Trondheim N–7491, Norway

ARTICLE INFO

Article history:
Received 22 March 2021
Received in revised form 2 July 2021
Accepted 3 July 2021
Available online 10 July 2021

Keywords:
Cliff failure
Back analysis
Climate change
Svalbard

ABSTRACT

Based on a morphostructural analysis of a cliff coast segment of Forkastningsfjellet, back analysis of the August 12th, 2016 rock slide situated at 78°19′10″N/15°39′52″E was carried out. This rock slide comprises a volume of 175,000 m^3, and indicates a partial reactivation at the front of the ~100 million m^3 large postglacial Forkastningsfjellet rock slide. We studied the controlling and triggering factors of the reactivation using a 2-D limit-equilibrium calculations and a 3-D simulation with Scoops3D. Slope instability initiated along a pre-existing listric block fault that was inherited from the postglacial Forkastningsfjellet rock slide. The cause of the failure is attributed to a strength decrease and additional water pressures along the pre-existing sliding plane, possibly in combination with a degradation of the affected weak shales of the Rurikfjellet Formation, which build up a major part of the steep slope.

Although the analysis suggests a structural control on the type and mechanism of slope failure, a significant impact of climate-related factors is inferred. Increasing temperatures and changing precipitation trends are reported from Svalbard. These are interpreted to foster permafrost degradation and reduce bonding forces in the thawing ice-filled fractures at the site. In addition, progressive weakening by more frequent frost and thaw cycles of the slaking shales and the introduction of additional water pressures to the rock mass are considered to contribute to the instability. The final trigger of the 2016 failure is attributed to a two-day rainfall that had preceded the event.

The application of the Scoops3D software tool showed that it is capable of predicting the locations and affected volumes of landslides with reasonable accuracy, when the geological and structural setting is well established. Under such premises the tool can be used to support preliminary susceptibility assessments in study areas with comparable geological and morphostructural settings.

1. Introduction

Landslides, defined as the movement of a mass of rock, debris, or earth down a slope, under the influence of gravity play an important role in the evolution of landscapes (Varnes, 1978; Dikau et al., 1996; Cruden and Varnes, 1996; Hungr et al., 2014). As a manifestation of slope instability, they directly modify the topography and in many areas pose a serious threat to the population (Glade and Crozier, 2005; Korup and Clague, 2009, Petley, 2012).

Slope failures are influenced by a variety of factors and conditions that can be differentiated into preconditioning, preparatory and triggering factors (Glade and Crozier, 2005; Hermanns et al., 2006; Crozier, 2010; McColl, 2012). Preconditions are static, inherent factors that are mainly defined by the rock mass properties. They are characterised by lithology and rock mass structure, i.e. the discontinuity system, and control the long-term slope stability and the adjustment of a stable slope geometry (Whalley, 1974; Hutchinson, 1988; Griffiths and Whitworth, 2012; McColl, 2012). However, with time a stable slope might be transferred into a marginally stable slope by acting preparatory factors like glacial erosion, rock stress redistribution or thermal effects. This will eventually lead to the final slope failure, which is often caused by an external stimulus (Cruden and Varnes, 1996; Wieczorek, 1996; Glade and Crozier, 2005). Understanding the contribution of influencing factors and the acting failure mechanism that drives the instability is essential to analyse the current state of slope stability, determine its sensitivity to different triggering mechanisms and to assess the hazard relating to a potentially unstable slope (Eberhardt et al., 2004; Glastonbury and Fell, 2010; Stead and Wolter, 2015).

In polar-and high mountain regions climate warming causes permafrost degradation and a change in the strength and temporal distribution of trigger mechanisms, such as precipitation distribution and intensity. This change has been shown to influence slope stability,

* Corresponding author at: Federal Institute for Geosciences and Natural Resources, Stilleweg 2, 30655 Hannover, Germany.
E-mail address: d.kuhn@bgr.de (D. Kuhn).

https://doi.org/10.1016/j.geomorph.2021.107850
0169-555X/

landscape evolution, and the natural hazard potential (Gruber and Haeberli, 2007; Borgatti and Soldati, 2010; Fischer et al., 2012; Huggel et al., 2012; McColl, 2012; Krautblatter et al., 2013; Blikra and Christiansen, 2014; Higman et al., 2018; McColl and Draebing, 2019; Svennevig et al., 2020; Bessette-Kirton and Coe, 2020).

On Svalbard, long-term climate observations show an increase in the mean temperature (Nordli et al., 2014), and projections of climate change scenarios predict a continued increase of annual temperatures and rainfall, leading to permafrost thaw, increased erosion, and sediment transport, among others (Hanssen-Bauer et al., 2019). Because meteorological factors are important triggers for all types of mass movements (e.g. Crozier, 1999; McInnes et al., 2007), an increase of active slope processes and significantly greater instability in the mountain slopes is likely (Hanssen-Bauer et al., 2019).

The Forkastningsfjellet mountain, situated 10 km from Svalbards largest settlement Longyearbyen, is a typical representative of a paraglacial landscape (Ballantyne, 2002; Ballantyne and Stone, 2013; McColl, 2012), characterised by the transition from glacial conditions to non-glacial conditions. The glacially-eroded mountain has experienced unstable conditions after deglaciation as indicated by a ~ 100 million m^3 rock slide (Major and Nagy, 1972; Dallmann et al., 2001; Albertsen, 2016; Kuhn et al., 2019), here after called "the postglacial rock slide". The resulting stair-stepped morphostructural relief is the result of this huge postglacial Forkastningsfjellet rock slide that developed in the hanging wall of a listric, northwest-dipping slide surface (Kuhn et al., 2019, 2020). This postglacial rock slide traveled to the west into the Isfjorden coastal area and was fragmented into tilt blocks of differing volumes and sizes. On August 12th, 2016 a rock slide occurred at 78°19′10"N/15°39′52″E. It shows that the postglacial rock slide is changing from a dormant to an active state. That could represent a threat to nearby Longyearbyen and therefore should be investigated.

Though, a structural control of rock slope instabilities has been observed in comparable morphostructural and climatic settings (Böhme et al., 2013, Böhme et al., 2011, Henderson and Saintot, 2011; Saintot et al., 2011, Vick et al., 2020), studies linking gravitational rock slope deformations with the inherited bedrock structure and deformation mechanisms on Svalbard are new. Also, the reactivation potential of large slide blocks of the Forkastningsfjellet rock slide along pre-existing sliding planes have not been explored so far. Such large-scale rock slope failures entering a fjord might generate large displacement waves that pose a threat to the marine traffic and inhabited surroundings in case that they are catastrophic (Hermanns et al. 2013; Gauthier et al. 2018).

In this paper, we present the results of a detailed investigation of the August, 8th 2016 rock slide which is the first reactivation of a dormant slide block of the postglacial rock slide deposit, and that is hereafter called "the recent rock slide".

This study aims to understand the characteristics of the recent rock slide and to draw conclusions about its causes, conditioning factors and triggers. We test our working hypothesis that the morphostructural inheritance of the rock slide deposit favours its recent reactivation by a 2-D back analysis. We also apply a 3-D approach with the software package Scoops 3D (Reid et al., 2000; Reid et al., 2015). This tool could help to assess and quantify both the locations of minimum slope stability and the expected volumes of potential failure and facilitate evaluations of landslide susceptibility. Also, it might help to understand if changing environmental conditions and correlated increasing water pressures cause the reactivation of the rock slide.

Such information is crucial to identify other metastable rock slope sections, both in the vicinity of the investigated rock slide (Kuhn et al., 2020) and along the entire Isfjorden coastline, that might fail unexpectedly as destructive rockslides in future. The latter would have a considerable impact on hazard and risk assessments for nearby harbour facilities, low lying infrastructure, houses and cabins as well as passing boats and visiting tourists.

2. Study area

2.1. Location and geological setting

Forkastningsfjellet is a narrow, NE–SW-oriented mountain ridge to the North of Longyearbyen, the capital of Svalbard (Fig. 1). The coastal mountain range reaches a maximum altitude of 490 m and is characterised by a rugged morphology, steep cliffs and many structural elements of tectonic origin. Well-bedded sedimentary rocks of the Upper Jurassic to Cretaceous Adventdalen Group (Parker, 1967; Major and Nagy, 1972; Dypvik et al., 1991; Dallmann et al., 2001) characterize the area. The rock sequence was differentiated into the lower Janusfjellet subgroup comprising mudstones and shales of the Agardhfjellet Formation (Jurassic) and the overlying Rurikfjellet Formation (Early Cretaceous). It is overlain by the deltaic Helvetiafjellet Formation with its lower cliff-forming sandstone unit of the Festningen Member. The top of the sequence comprises alternating sandstones and mudstones of the heterolithic Carolinefjellet Formation (Parker, 1967).

At Forkastningsfjellet, the sequence was affected by two different deformation phases that formed the dominant morphostructural features of the ridge (Dallmann et al., 2001; Albertsen, 2016; Kuhn et al., 2019). During the first tectonic deformation phase in the Eocene, the rocks were affected by thin-skinned deformation leading to NE- and SW-vergent folding and thrust faulting attributed to the development of the transpressional West Spitsbergen Fold-and-Thrust Belt along the western coast of Spitsbergen (Bergh et al., 1997; Tessensohn and Piepjohn, 2000; Dallmann et al., 2001). The second deformation phase was a postglacial, gravitationally driven, extensional deformation, that was offsetting rock slide blocks in the hanging wall of a listric NW-dipping rupture surface. The failure or sequence of failures split up the rock mass into seventeen differently-sized fault blocks which govern the pronounced local relief and define the coastal ridge (Kuhn et al. 2019, 2020) (Fig. 2). Kuhn et al. (2019) divided the postglacial rock slide in a northern, central and southern segment. The recent rockslide occurred at the transition from the central to the northern segment.

Active mass wasting occurs in all segments of the postglacial rock slide. The western flats and slopes are affected by superficial active-layer detachments (ALD) and debris flows, while the steep slopes of the coastal tilt blocks show rock falls and translational failures parallel to the cliff.

The recent slope failure along these coastal blocks drew attention to the stability and the potential landslide hazard along the Forkastningsfjellet cliff line. This failure is so far the largest recent reactivation and affected the coastal cliff face of Block 10 in the northern segment adjacent to block 12 in the central segment (Fig. 3).

2.2. Climate, permafrost and active layer thickness

The climate in the central part of Spitsbergen is arctic, and the mean annual air temperature measured at the Svalbard Airport, Longyearbyen (approximately 9 km south of the study area) is −5.9 °C (1971–2000). Mean annual precipitation (1971–2000) is 196 mm (Hanssen-Bauer et al., 2019).

However, for the period 1971–2017 the mean annual air temperature in Svalbard has increased by 3 °C to 5 °C (Førland et al., 2011; Hanssen-Bauer et al., 2019). This is triple or more from the global mean temperature rise. Temperature projections imply also no change for the future in this trend and a further increase in the number of thermal growing days and a decrease in the number of frost days (Førland et al., 2011; Hanssen-Bauer et al., 2019).

This goes along with an increase in annual precipitation measured at Svalbard Airport, that indicates an annual average increase of 2% per decade (Førland et al., 2011).

Permafrost in Svalbard is typically about 100 m thick in the valleys and near the coast and 400–500 m thick in the mountains (Humlum et al., 2003; Christiansen et al., 2010). It is overlain by a 0.8 to 2.5 m thick active layer between the surface and permafrost that undergoes

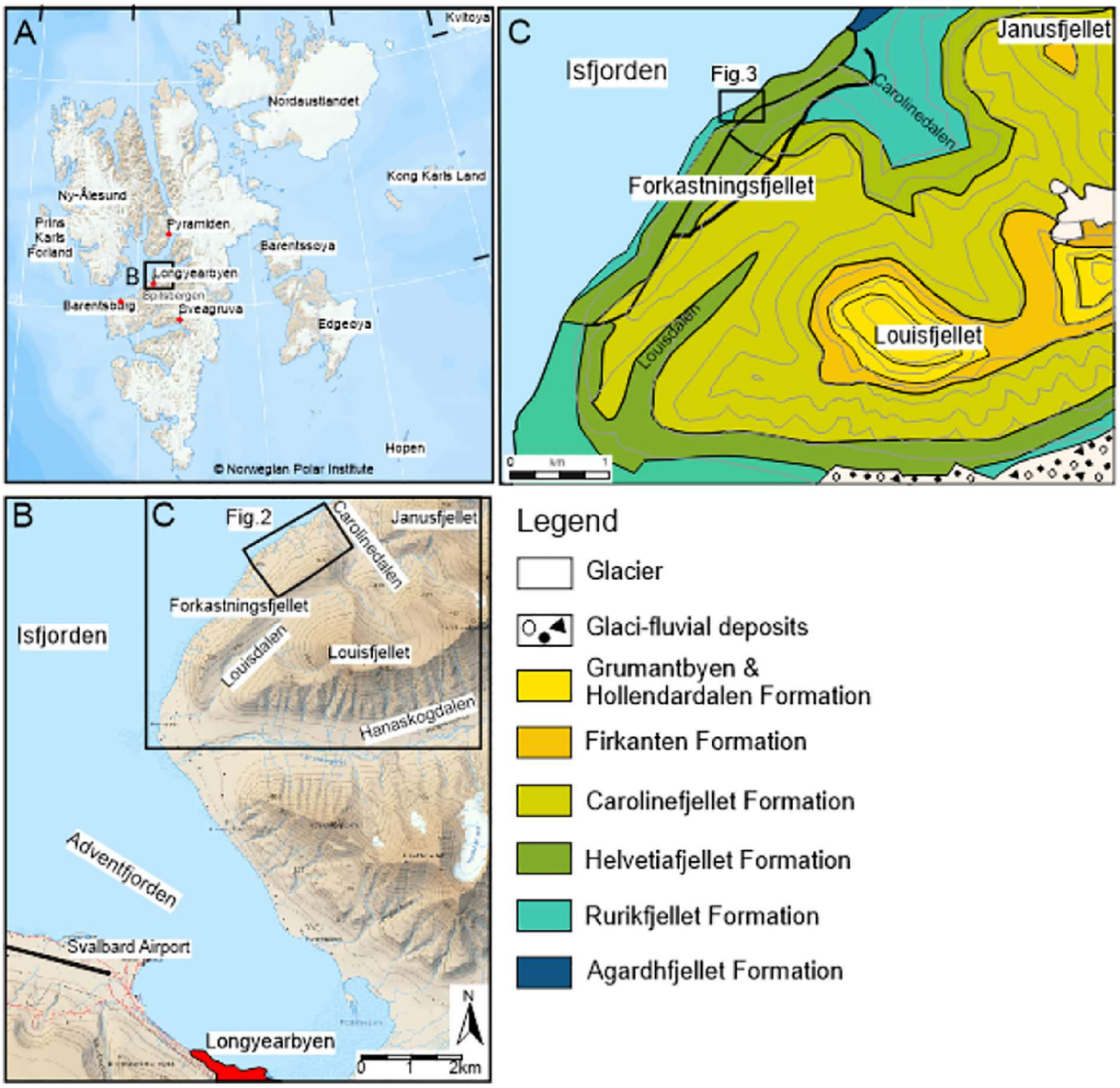

Fig. 1. (a) Overview map of Svalbard, (b) regional over-view map of the working area, (c) geological map of the Forkastningsfjellet region (Norsk Polarinstitutt, 2018).

seasonal freezing and thawing (Christiansen et al., 2010). Time series of active-layer thickness and permafrost temperature conditions in Svalbard show generally increasing active-layer depths and rising permafrost temperatures (Isaksen et al., 2007; Harris et al., 2011; Christiansen et al., 2010).

The observed warming trend and changing weather characteristics with increasing annual air temperature, increasing annual precipitation and more frequent high-intensity rainfall events have a substantial impact on geomorphic processes in Svalbard and raise concerns related to the stability of slopes and existing infrastructure (Hartvich et al., 2017; Hanssen-Bauer et al., 2019; Gilbert et al., 2019).

3. Methods

3.1. Field mapping and rock slide volume estimation

Detailed geomorphological and structural field mapping was conducted using an existing geological map at a 1:100,000 scale (Sheet C9G Adventdalen; Dallmann et al., 2001) and a digital elevation model (DEM) acquired in 2009 with a grid size of 5 m × 5 m (Norsk Polarinstitutt, 2018). In the course of a flight campaign with an unmanned airborne vehicle (UAV) in summer 2019, high-resolution stereo images were acquired. We deployed a DJI Phantom 4 RTK drone, and the images were processed with the DJI Terra Pro software (DJI, 2021). The resulting DEM has a spatial resolution of 0.25 m. Overlay of the different DEMs was used for change detection of the affected slope area and volume estimation of the rock slide. For the latter, we resampled the DEMs of 2009 and 2019 to a spatial resolution of 1 m and calculated the difference in the GIS (Fig. 4).

3.2. 2-D back analysis of the rock slide

For the 2-D back analysis of the investigated rock slide, DEM-based cross-sections were constructed, and slope stability calculations were performed to determine the shear strength parameters and the geotechnical and environmental conditions under which failure may have occurred. We used a circular shape as the critical slip surface and Bishop's modified methodology of limit equilibrium analysis to calculate the Factor of Safety (FOS) (Bishop, 1955). A circular surface is

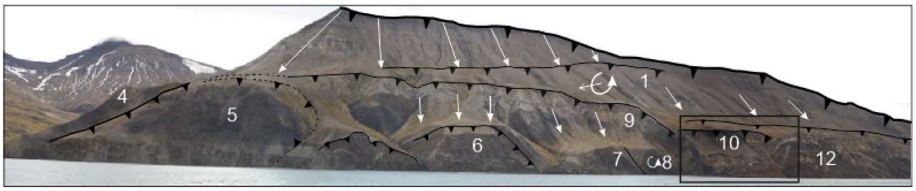

Fig. 2. The northern segment of Forkastningsfjellet rock slide, view to the east. The slide mass disintegrated into several slide blocks, which are marked with white numbers (Kuhn et al., 2019). On August 08th, 2016, Block 10, situated at the transition from the northern to the central segment, was affected by a large landslide with an estimated volume of 200,000 m^3 (framed area, shown in Fig. 3).

justified based on field observations, showing that the inherited slide block boundaries of the postglacial rock slide have a listric shape (see below).

The procedure involved the subdivision of the sliding mass into a series of slices and the iterative calculation of specific static equilibrium equations (Duncan, 1996; Duncan et al., 2014). The calculation was done manually using a spreadsheet application.

The FOS is defined as the ratio of the shear strength divided by the shear stress required for the equilibrium of the slope (Wyllie and Mah, 2004):

$$FOS = \frac{\textit{shear strength available to resist sliding}}{\textit{shear stress required for equilibrium on slip surface}} = \frac{c + \sigma tan\Phi}{\tau\ \mathrm{eq}} \quad (1)$$

with cohesion c, friction angle ϕ, shear strength τ, and σ as the total normal stress on the sliding plane. If the shear strength is expressed in terms of effective stresses, i.e., groundwater pressures are involved, the above-mentioned equation can be written as:

$$\tau = \frac{c\prime + (\sigma\prime - u)tan\phi}{F} \quad (2)$$

where c' and ϕ' represent the shear strength parameters in terms of effective stresses, and u is the water pressure. After Duncan (1996) the FOS can then be calculated using the following expressions:

$$N1 = Wsin\alpha \quad (3)$$

$$N2 = \frac{\left\{\left[\frac{W}{cos\alpha} - ul\right]tan\phi + cl\right\}}{\left[1 + \frac{tan\alpha\ tan\phi}{Fa}\right]} \quad (4)$$

$$Fc = \sum(N2)/\sum(N1) \quad (5)$$

where

W = weight of slice – kN/m.

c = cohesion – kN/m^2.

φ = friction angle - degrees.

α = angle between the base of slice and horizontal – degrees.

u = pore pressure – kN/m^2.

l = length of slip surface segments measured along the base of slice - m.

Fa = assumed FOS Fc = calculated FOS.

Because the normal force in *N2* (Eq. (4)) depends on FOS, while the FOS (Eq. (5)) also depends on *N2,* it is necessary to use repeated trials to calculate the factor *of* safety by Bishop's modified method (Duncan, 1996; Duncan et al., 2014).

3.3. Stability analysis with Scoops 3D

Using the derived shear strength parameters of the 2-D analysis, the software package Scoops 3D (Reid et al., 2000; Reid et al., 2015) was applied to explore the potential and applicability of the approach to support preliminary evaluations of possible landslide reactivations along the Forkastningsfjellet.

Based on a digital terrain model, the deterministic Scoops3D software uses a three-dimensional (3-D) method of columns limit-equilibrium approach to perform a comprehensive three-dimensional slope stability analysis. The tool systematically searches a digital landscape and computes the stability of 3-D potential landslides, assuming rotational slip and encompassing a wide range of depths and volumes that potentially affect different parts of the DEM. For each potential landslide, Scoops3D assesses the stability of a rotational, spherical slip surface using a 3-D version of Bishop's simplified method of limit-equilibrium analysis.

Given the required input data, e.g., the DEM, the material properties or the pore water pressure conditions, the software calculates the factor of safety (FOS) of each potential slip surface. It provides a 3-D distribution of stability underlying the DEM that can be visualised in any GIS supporting raster formats (Reid et al., 2015). The mathematical derivation and conversion of Bishop's method from 2-D to 3-D is not presented here, and the reader is referred to the original publication of Reid et al. (2015).

Fig. 3. The landslide site, August 30th, 2019, view to the east. The uppermost 30 m of the main scarp is composed of a well-bedded sequence of sandstones and siltstones with closely spaced persistent joints. Slabs of the former land surface are visible on top of the downthrown mass (red arrow). Isolated rock towers ready to topple (orange arrow) and cracks at the landslide crown indicate an active retrogression of the main scarp to the East. Note the rotated sedimentary sequence of Block 12 and the flat-lying beds at the landslide crown of Block 10.

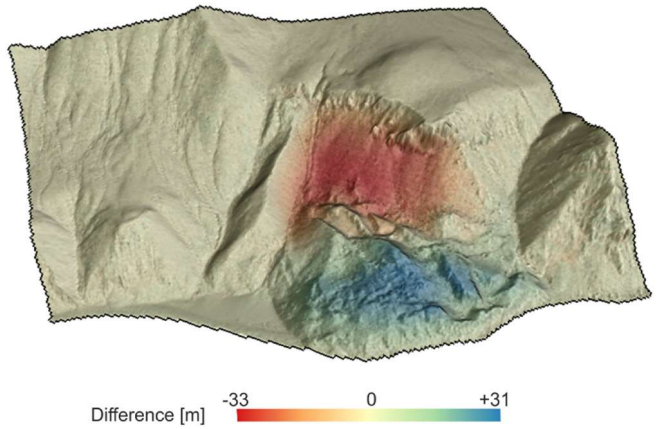

Fig. 4. Calculation of the rock slide volume by differential analysis of two DEM's of 2009 (Norsk Polarinstitutt, 2018) and the newly created UAV-DEM of 2019 (Kuhn et al. 2020). Red to orange colours show the depletion zone, green to blue colours indicate the accumulation zone.

3.4. Weather statistics

To analyse the weather condition before and during the rock slide failure in August 2016 we used weather data provided by Norsk Klimaservicecenter (https://klimaservicesenter.no), which are the mean air temperatures (24 h) and mean precipitation (24 h) from the meteorological station Svalbard Airport, situated 9 km southwest of the landslide site.

4. Analysis and results

4.1. Field mapping and rock slide volume estimation

4.1.1. Detailed description of Landslide area and event

The landslide area exhibits a complex structural assemblage of slide blocks with steep slopes, which are part of the downthrown slide mass of the postglacial Forkastningsfjellet rock slide (Fig. 2; Kuhn et al., 2019, 2020). On August 8th, 2016, between 4 and 6 p.m., a section of the Forkastningsfjellet cliff coast (78°19′10"N/15°39′52″E) was affected by a rotational rock slide (Røsvik, 2016; Fig. 3). The failure occurred on the coastal face of Block 10 (following the numbering of Kuhn et al., 2019), situated in the transition area between the northern and central segment of the postglacial Forkastningsfjellet rock slide (Figs. 2, 3).

A former preliminary field assessment of the landslide volume was 300,000 m^3 (Kuhn et al., 2019) and is herewith reduced to a maximum of 175,000 m^3, based on differential analysis of two digital elevation models (DEM) of 2009 (Norsk Polarinstitutt, 2018; grid size of 5 m × 5 m) and the newly created UAV-DEM of summer 2019 (Kuhn et al. 2020; grid size of 0.25 m × 0.25 m). After resampling of the DEMs of 2009 and 2019 to a spatial resolution of 1 m the sum for all pixel values belonging either to the depletion or accumulation zone of the mass movement area were calculated. We differentiated 175,000 m^3 material which was detached from the depletion zone and a volume of 166,000 m^3 material that was deposited in the accumulation zone (Fig. 4). The difference of 9000 m^3 is assigned to 3 years of coastal erosion since the rock slide occurred.

During the westward downslope movement along the NNW-dipping listric failure surface, the failed rock mass was fragmented into slabs and rotated slices of rock and settled with a stepped hemispherical outline on the shore platform of Isfjorden. In total, the landslide deposit traveled at least 200 m in NNW-direction (Fig. 6). Block 10 is composed of the well-bedded and flat-lying succession of shales and mudstones of the Rurikfjellet Formation, and the overlying Helvetiafjellet Formation with its cliff-forming lower sandstones of the Festningen Member (grey sandstone bed in Fig. 3) and overlying coal-bearing shales and sandstones of the Glitrefjellet Member (Parker, 1967; Gjelberg and Steel, 1995; Midtkandal et al., 2008).

In contrast, the outcropping sedimentary sequence of the neighboring Block 12 to the south shows a strong bedding inclination (bedding 48/35 SE). A fractured wedge-shaped rock body in the fault zone between Block 10 and Block 12 (Fig. 6) indicates that the landslide affected an extensional fault zone between the blocks, which were juxtaposed during the postglacial Forkastningsfjellet rock slide. Such a complicated structural arrangement of the different rock slide blocks has substantial implications on the causes and kinematics of the landslide. Therefore, the following section presents the initial pre-landslide situation in detail.

4.1.2. Temporal development of the landslide area

To understand the initial morphostructural setting of the pre-failure slope and support the working hypothesis, we compared and interpreted a set of multitemporal air photos (Fig. 7).

Fig. 6 A shows the pre-failure situation of Block 10 (Acquisition date 06.07.2016; A. Skoglund/Norsk Polarinstitutt). Before the recent rock slide the slope face was formed by a heterogeneous rock mass consisting of well-bedded and fractured sand- and siltstones at the upper third of the face, the NE-dipping rotated sequence of grey sandstones and black shales with intercalated coal layers in the middle part of the slope, and the relatively weak shales and siltstones at the bottom. The same sequence is observed in the top section of neighboring back-rotated Block 12 to the south, though with a different altitude.

We interpret this rotated sequence in the middle and lower part of Block 10 as the remnants of the northern extension of Block 12, which was initially in fault contact with Block 10 (Fig. 8). The two identified fault contacts shown in Fig. 8 support this interpretation. A fault-bounded wedge-shaped rock sliver borders the tilted Block 12 to the West. This imbricated rock sliver can be traced to the southern segment of the main scarp, where a small fragment of the rock sliver is still attached to Block 10. These observations prove that Block 12 was originally larger and extended farther to the North, where it was attached along a fault contact to Block 10.

Consequently, we conclude that the downthrown landslide mass failed along an older pre-existing west-dipping sliding plane, which is attributed to the older Forkastningsfjellet rock slide event and juxtaposed Block 10 and the former larger slide block Block 12.

Based on the multitemporal air photo analysis, we were able to reconstruct the following sequence of events.

In the course of the sliding event, the rock face consisting of the remnants of Block 12 failed along the steep west-dipping listric block fault

Fig. 5. Central part of the rock slide head showing the back rotated blocks to the left and the central block that moved about 40–50 m almost vertically down thereby sustaining the original orientation of the cliff-top drainage rills (view to the North).

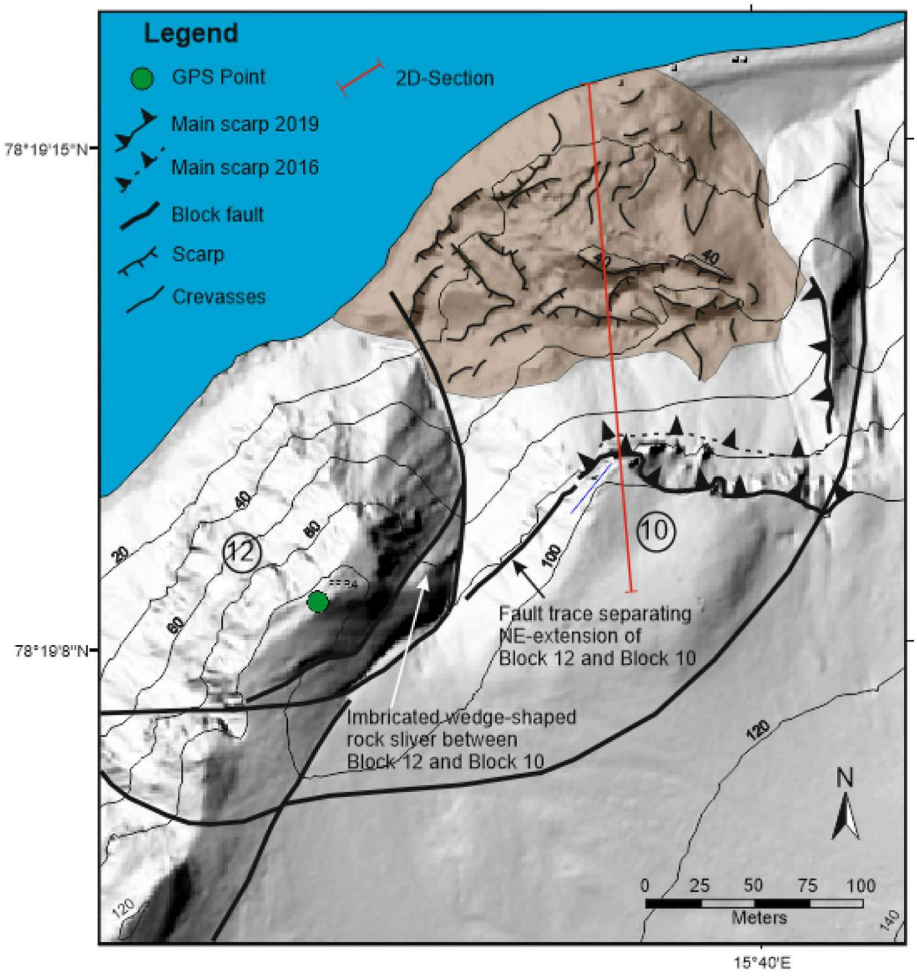

Fig. 6. Map of the rock slide area, showing the inherited block bounding fault system and the rockslide with features discussed in the text.

that served as a zone of weakness (Fig. 7B). Laterally, the landslide is limited to the south by a narrow valley that drains the higher plateau to the east. To the North, a new steep scarp developed in an unstructured former slope deposit interpreted as remnants of a northern neighboring fault block and erosional debris from the steep slopes to the East (Fig. 6). In plan view, the crown escarpment initially showed a division in segments, which developed along intersecting major joints and tension cracks. In the following year (between August 2016 and July 2017), the head scarp migrated eastward and affected the closely fractured cap rocks of Block 10.

The initial frayed asymmetry of the scarp was smoothed by further minor failures. The detachment of overhanging rock fragments led to further retrogression of the central and NW-part of the crown scarp (Fig. 7C), and a new NE-SW oriented 100 m long rupture surface was created (Fig. 3; Fig. 7C).

Between July 2018 and August 2019, the continued eastward retrogression of the crown scarp was most efficient along the central and NE-extension of the scarp. In contrast, the SW-edge stayed behind, and a protruding spur of intensely fractured sandstone that builds the surface of the block was created (Fig. 7D).

During field inspection in August 2019, arcuate extensional cracks affecting the landslide crest and toppling rock towers beneath the crown were observed, indicating a continued landward extension of the landslide to the East.

4.1.3. Characteristics of scarp and displaced material

During field inspection, only the uppermost 20 m of the landslide scarp were visually observable. Direct measurements of the joint system were impossible due to intense rock fall activity and inaccessibility of the steep slope. Therefore, the description of the rock slide crown was derived from photo interpretation and the UAV-based air photos.

Fig. 7B shows that the main scarp cut the upper part of the slope along the steeply dipping, narrow spaced fracture system and curved downwards into a listric sliding surface currently covered by rock fall debris (Fig. 7C, Fig. 7D). The crest section is characterised by a sequence of well-bedded flat-lying sandstones and siltstones with intercalated mudstones that are affected by several sets of planar and subvertically oriented joints. Besides the flat-lying bedding planes, the most prominent joint system is a conjugate set of steeply dipping joints striking 40° and 130°. Additional fracture sets with deviating orientation and lower persistence result in a closely fractured rock mass (Fig. 9).

Due to the pervasive fracture system, the crest section shows a rough irregular contour with angular and wedge-shaped break-outs, governed by the intersecting joints that act as releasing surfaces.

Below this vertical section, the rupture surface continues as a stepped discontinuous plane consisting of steep sections affecting the stronger sandstones and flat sections in the weak shale beds that are characterised by extensional displacement and shear displacement, respectively (Fig. 7B; Fig. 9). Interpretation of Fig. 7B indicates that this sequence of steep and flat segments continues downwards into the listric lower part of the rupture surface. The latter lower part of the rupture surface was covered by talus and debris, which inhibited direct inspection. It is assumed that the rupture surface daylighted at the toe of the slope. Therefore, we deduced an overall listric shape of the slide surface.

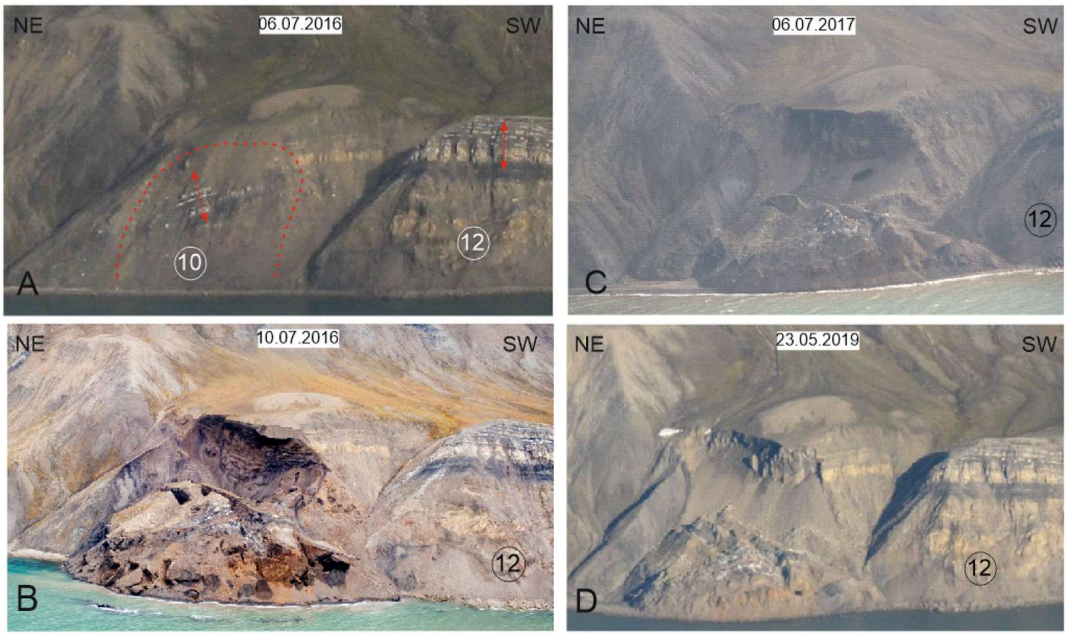

Fig. 7. Development of the landslide area with time. A: Pre-failure slope morphology of Block 10. The upper third of the face shows a heterogeneous sequence with flat-lying beds of sand- and siltstones and a NE-dipping (rotated) interbedded sequence of grey sandstones and black shales with coal layers in the middle part of the slope. The same alternating sandstone-shale succession is discernible on the top of Block 12 (compare red arrows). Therefore, the rotated NW-dipping sequence is interpreted as the remnants of the northern extension of Block 12, which was in fault contact with Block 10 (Photo: A. Skoglund/Norsk Polarinstitutt, Acquisition date 06.07.2016). B) Situation four days after the rock slide occurred. The rupture surface shows a stepped outline with steep sections affecting the stronger sandstones and flat slide sections in the soft shale beds (Photo: Røsvik, 2016; Acquisition date 12.08.2016). C: State of the landslide on 06.07.2017. Subsequent minor failures along the closely fractured cap rock led to eastward head propagation and straightened the crown escarpment (Photo: A. Skoglund/Norsk Polarinstitutt). D: State of the landslide on 23.05.2019. Talus cones of rock debris from the upper bedrock cover the slide plane. Note the toppling rock towers formed by intersecting fracture planes and continued relaxation of the main scarp (Photo: A. Skoglund/Norsk Polarinstitutt).

In the central part, the head of the displaced rock mass moved about 40–50 m almost vertically down thereby sustaining the original orientation of the cliff-top drainage rills with a backward tilt (Fig. 5).

Farther downslope, the movement in the hanging wall of the listric concave segment of the rupture surface led to the separation of the slide mass into elongated slabs and juxtaposed back rotated angular blocks, which floated in a coarse granular unstructured mass. The toe of the displaced rock mass entered the sea, so the measured travel distance of 200 m in NW-direction is assumed a minimum value.

4.1.4. Rock slide classification and mechanism

Based on the described field observations, we define the event as a rotational rock slide that initiated along a pre-existing listric extensional Block fault. This inherited plane of weakness was created during the post-glacial Forkastningsfjellet rock slide and separated the two coastal blocks, Block 10 and Block 12. Reactivation of this former sliding plane led to the main failure event. Subsequently, and due to the lacking support from below, the more rigid cap rock failed along the closely spaced joint system. This adjustment to the new slope stability conditions resulted in a southeastward migration of the rock slide crown, and this active extension, including rock fall and toppling rock towers, still continues.

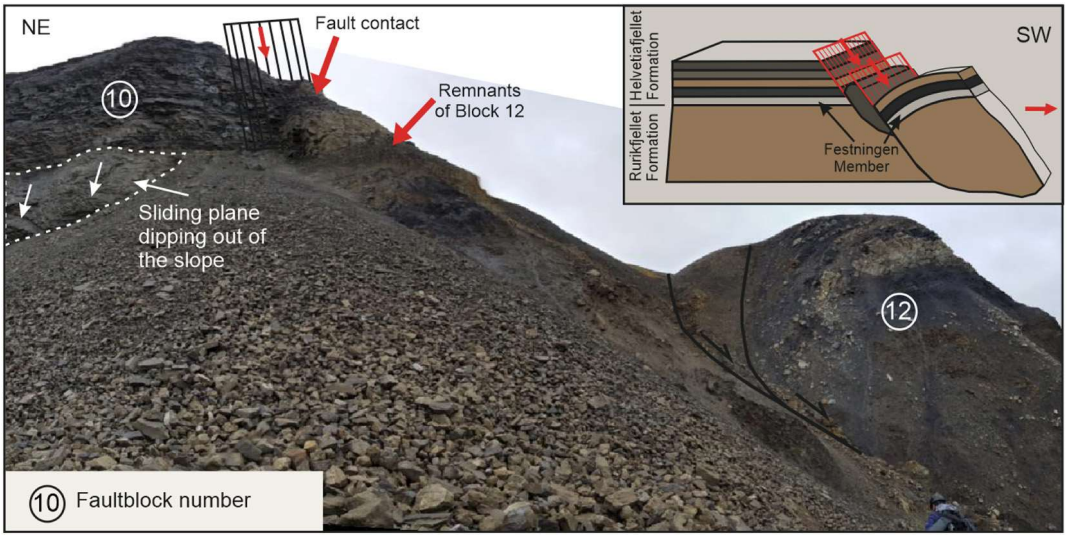

Fig. 8. Actual scarp and fault contact of the slide blocks. The left and central part of the photo shows the crown scarp with a flat-lying sandstone-shale sequence of Block 10 and attached remnants of the former northern extension of Block 12. Farther to the right, a wedge-shaped rock sliver marks the fault contact between Block 10 and Block 12 with the back rotated sedimentary sequence (bedding 148/45SE). Note person at the lower right margin for scale.

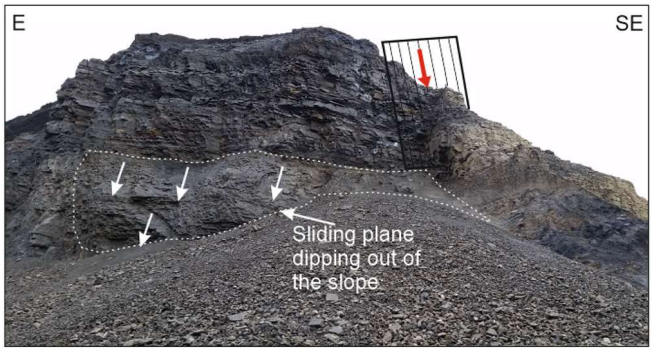

Fig. 9. Section of the slope parallel west-dipping surface of rupture observed in August 2017. The smooth wavy surface (white stippled outline) dips out of the slope and shows a stepped surface comprising extensional steep dipping joints separated by portions of sheared rock bridges. The fault plane can be traced into the fault contact between Block 10 and Block 12 to the southeast (Fig. 8). It ends along a subvertical break-off and continues below the talus and the rock slide deposits.

4.2. 2-D Back analysis of the rock slide

To assess the failure conditions and deduce the shear strength parameters friction angle φ and cohesion c of the rupture surface during failure (factor of safety (FOS) = 1) we conducted a limit equilibrium analysis based on the method of Bishop. The calculations also served to derive the necessary input parameters for the subsequent 3-D analysis.

4.2.1. Input parameter and analysis procedure

In the first step, a 2-D cross-section of the central part of the rock slide was created. This is the part of the rock slide with the longest estimated transport distance of the failed rock mass and the smallest changes since 2016 (Fig. 6). The slope shape used for the pre-failure situation was obtained from the 2009 DEM, the post-failure situation was derived from the UAV-based DEM of 2019 (Fig. 10). Additionally, the air photo of August 2016 provided rough constraints for delineation of the initial failure. The slide mass was reconstructed and subdivided into 18 vertical slices (Fig. 10).

The available geotechnical information on the material properties of the rock formations affected by the rock slide is limited. No information was available for the Helvetiafjellet Formation and the intercalated sandstone units of the Rurikfjellet Formation. Bohloli et al. (2014, 2015) conducted laboratory tests on shale samples of the Rurikfjellet Formation taken from boreholes (depth interval of 367–384 m). They report a density of 2.6 g/cm^3, a cohesion of 3.2 MPa, and friction angles of 16°. These values have been derived for fresh, unweathered borehole samples and do not apply to the outcropping weathered and fractured shales in the working area. Especially the very high value for cohesion would inhibit any slope instability. Therefore, the test trials used published values for soft jointed rock masses, with cohesion ranging between 0 and 200 kPa and friction angles ranging between 15 and 25° (Hoek and Bray, 1981; Wyllie and Mah, 2004). The unit weight of the rock mass (including thin coal seams) was set to the average value of 25 kN/m^3.

Sequential calculations were performed in a spreadsheet application with varying geotechnical properties for cohesion c and friction angle φ. To approximate the conditions for slope failure, i.e., for a FOS = 1, several iterations were needed for the calculation, starting with an assumed FOS (Fa) = 1. The resulting calculated value of FOS (Fc) was then used as Fa for the next iteration. This procedure continued until the assumed, and calculated values of Fa and Fc were equal.

As groundwater pressure measurements within the slope are not available and the permafrost depth is unknown, a total stress analysis without pore pressure was performed in the first step.

In a second approach, we applied a water pressure ratio $r_u = 0.1$, i.e. a 10% of the total stresses, to consider the fact that the slopes thaw in the summer and free water can seep into the slope. After Bishop and Morgenstern (1960), r_u is defined as the pore pressure ratio.

$$r_u = \frac{u}{\gamma z} \tag{6}$$

where

u = water pressure – kN/m^2.

z = length of slip surface segments measured along the base of slice – m.

γ = unit weight of rock - kN/m^3.

z = height of slice - m.

4.2.2. 2-D slope stability calculation

Several calculations were made to approximate the shear strength properties during slope failure, comprising both dry conditions (no water pressure, $r_u = 0$) and an existing water pressure acting along the sliding plane. A selection of the results of the calculations is summarised in Table 1.

Best results for failure under dry conditions were obtained for the cohesion/friction angle value pairs of 130 kPa/20° and 150 kPa/15°.

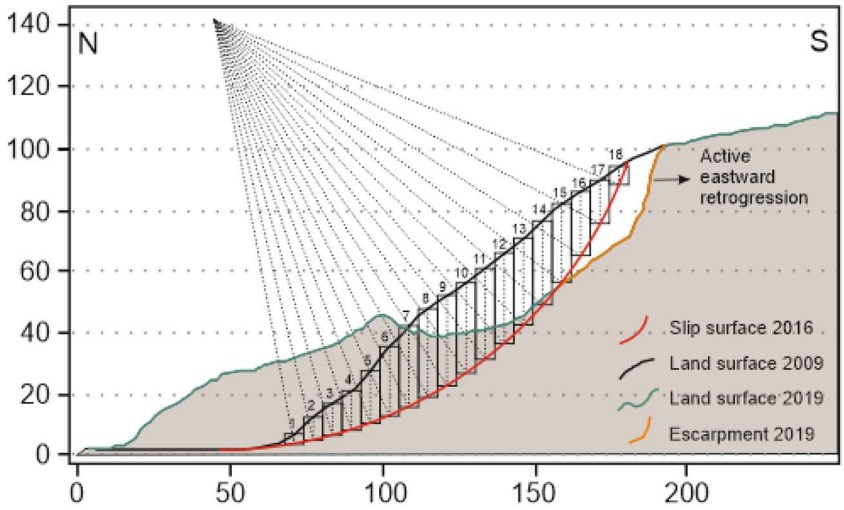

Fig. 10. 2-D stability analysis performed for a section through the center of the rock slide and using the pre- and post-event slope morphology deduced from the DEMs of 2009 and 2019 (Fig. 6). The circular slip surface was derived from the visual air photo interpretation of August 2016.

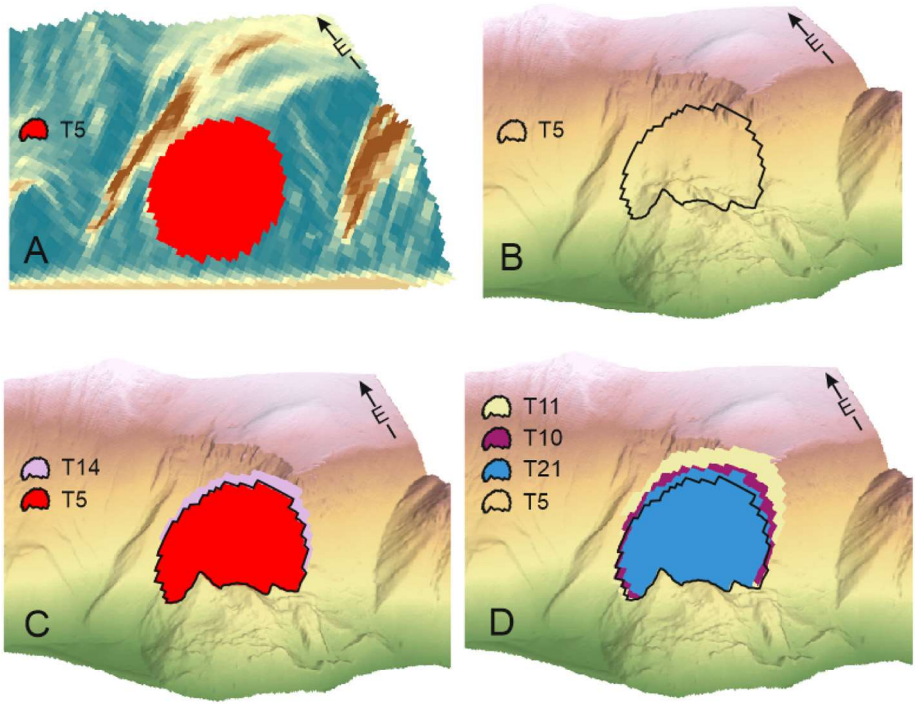

Fig. 11. Perspective views showing stability calculation results from the Scoops3D analysis, which are draped on the DEM. A) Initial slope topography derived from DEM of 2009 with the area of the potential slope failure of Trial 5 (FOS = 1,05) in red. B) DEM of 2019 with the potential slope failure outline of Trial 5. C) The best-fit slip surfaces for calculations with $r_u = 0.1$ and $r_u = 0$. D) Three potential slip surfaces for the c = 0 kPa calculations (T10, T11, T25), the black outline shows the extension of the best fit result of Trial 5 for comparison.

Using effective stress conditions with an assumed water pressure of 10% of the total stress ($r_u = 0.1$) on the sliding plane, the best approximation to FOS = 1 was obtained for the cohesion/friction angle value pairs of 175 kPa/15° and 150 kPa/20°.

The back-calculation was also performed for a negligible cohesion of c = 0 MPa, which is the general assumption for active rock slides. Under this premise, failure under dry conditions requires a friction angle of 35° on the sliding plane. With the assumption of water pressure, even an unrealistic friction angle of >40° was not sufficient to calculate slope stability with a FOS = 1.

4.3. 3-D Back analysis with Scoops3D

4.3.1. Input parameter and analysis procedure

For the investigation, we used the strength parameter of the 2-D analysis and published values for soft jointed rock masses, with cohesion ranging between 0 and 200 kPa and friction angles ranging between 15 and 25° (Hoek and Bray, 1981; Wyllie and Mah, 2004). Again, the unit weight of the rock mass was set to an averaged value of 25 kN/m^3, and we investigated dry ($r_u = 0.1$) and wet conditions applying a pore pressure ratio $r_u = 0.1$. The ranges of the properties used in the study are shown in Table 2.

Slope stability calculations were performed using the DEM of 2009 (5 m pixel size) that represents the pre-rock slide topography of the rock slide area. The analysis started with the input of subsurface parameters and the definition of the search configuration.

Given the extension of the initial landslide scarp and an estimated rock slide volume of 175,000 m^3–200,000 m^3 (175k–200k), a series of slope stability calculations with variable geotechnical properties of the rock mass and varying size limits of the potential failure volumes was performed.

In a second step, the spatial extent of the calculated slip surfaces with the associated FOS between 0.93 and 1.1 were compared with the known outline and extension of the main scarp in the GIS

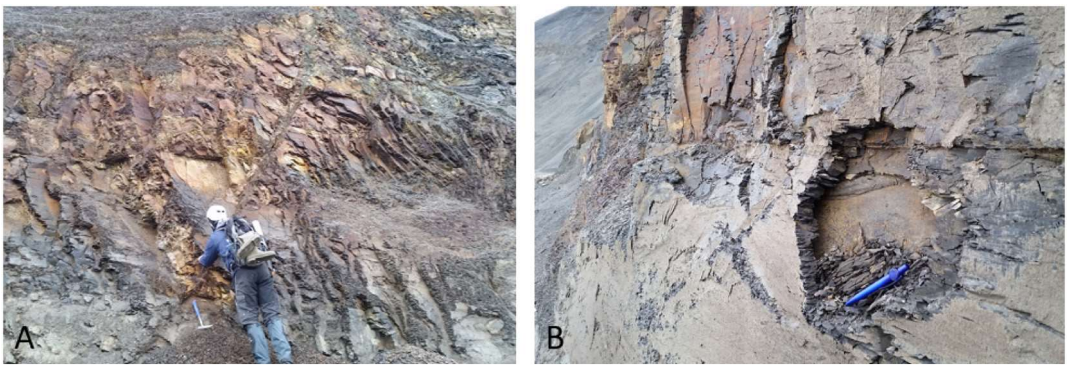

Fig. 12. A) Slope parallel sheeting joints and B) spalling affecting durable shales at the toe of the cliff faces. The adversely oriented sheeting joints favor slope parallel mass wasting along the coastal scarp.

Fig. 13. Rock fall fragment with ice-filled cracks from the active upper rock face of the rock slide, indicating weakening of the rock mass by melting of ice-bonded joints.

(Table 2; Fig. 10). Based on this best fit comparison we deduced the appropriate set of the associated shear strength properties for the respective slip surfaces.

4.3.2. Slope stability calculations with Scoops3D

A selection of the calculation's results, including strength parameters, affected volume and slip circle parameter are summarised in Table 3 and shown in Fig. 11.

Under effective stress conditions, the most significant degree of agreement between the calculated and the observed slip surface was found for Trial 5 with the cohesion/friction angle value pair of 130 kPa/15° and a water pressure ratio $r_u = 0.1$ (Fig. 11C). Differing parameter combinations led to mismatching slip surfaces, deviating volume calculations and/or FOS values beyond the specified range 0.93 and 1.1.

For conditions without water pressure ($r_u = 0$), an exact agreement between the calculated and observed slip surface could not be reached. The best approximation was obtained for Trial 14 with the cohesion/friction angle value pair of 120 kPa/15°, though the slip surface is too big and slightly displaced to the SW (Fig. 11C).

During the calculations, it turned out that the size limits of the potential failure volume greatly influence the extent of the potential slip surface. In general, the best agreement between the calculated and the observed slip surfaces was found for an upper search limit of 175,000 m^3. In contrast, the analysis with a maximum search volume of 200,000 m^3 yielded an areal mismatch and an excessive expansion of the slip surface to the southwest.

For calculations with negligible cohesion c = 0 kPa and water pressure ratio $r_u = 0.1$, no agreement was achieved between the predicted and the observed slip surface (Fig. 11D). For dry conditions, the best areal agreement was calculated for Trial 21, revealing a cohesion/friction angle value pair of 0 kPa /15°.

5. Discussion

The objective of this study has been to understand the characteristics of the latest rock slope failure and to draw conclusions about the causes and triggers of the reactivation of the postglacial Forkastningsfjellet failure. Such knowledge is necessary to transfer analysis results to the remaining fault blocks of the postglacial Forkastningsfjellet rock slide and identify sites with a potential for hazardous events in the near future. This is important as large scale rock slope failures entering the fjord might generate large displacement waves that pose a serious threat to the marine traffic and inhabited surroundings (e.g. Hermanns and Longva, 2012; Hermanns et al. 2013, Gauthier et al., 2018).

5.1. Controlling factors of instability

5.1.1. Role of structural predisposition on slope stability

Rock slope stability is governed by slope angle, slope height and the rock-mass strength, which is primarily determined by the rock properties and characteristics of the discontinuity system in the rock mass (e.g. Hoek and Bray, 1981; Cruden and Varnes, 1996; Hoek and Brown, 1997; Wyllie and Mah, 2004). It is generally accepted that structural heterogeneities, such as inherited tectonic faults and fractures play an important role in gravitational slope failure processes and may at least partly control the failure surfaces (Varnes, 1978; Jaboyedoff et al., 2009; Glastonbury and Fell, 2010; Saintot et al., 2011; Stead and Wolter, 2015; Vick et al., 2020).

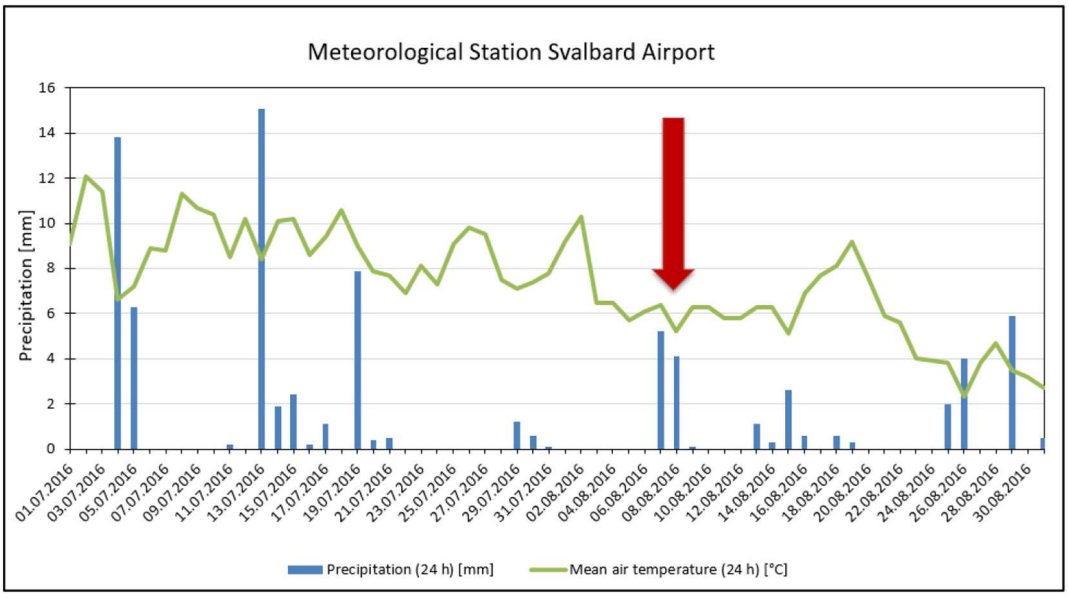

Fig. 14. Mean air temperatures (24 h) and precipitation (24 h) measured at meteorological station Svalbard Airport, situated 9 km southwest of the landslide site. Red arrow marks the measured precipitation and temperature before and during the landslide event (Source: Norsk Klimaservicecenter, https://klimaservicesenter.no).

Table 1
Selected results of the spreadsheet calculations with a unit weight of rock set to 25 kN/m^3 and variable values for cohesion c and friction angle φ. FOS is the final FOS (Fc) was obtained after four iterations.

Trial	Cohesion	Friction angle	r_u	FOS
	c [kN/m^2]	φ [°]		
1	0	30	–	0.83
2	0	35	–	1.0
3	0	40	–	1.19
4	150	20	–	1.18
5	130	20	–	1.09
6	175	15	–	1.15
7	150	15	–	1.04
8	130	15	–	0.96
9	0	35	0.1	0.72
10	0	40	0.1	0.85
11	150	16	0.1	0.95
12	150	20	0.1	1.03
13	175	20	0.1	1.13
14	175	15	0.1	1.04
15	150	15	0.1	0.93
16	130	15	0.1	0.84

At the rock slide site, field evidence showed that the failed slope segment consisted of a heterogeneous, tectonically stressed sequence of alternating shales and sand- and siltstones with different geotechnical parameters and varying degrees of weathering. Moreover, an older pre-existing block fault that separated the northern extension of Block 12 from Block 10 was identified. This block fault was initiated as a sliding plane during the postglacial Forkastningsfjellet rock slide event (Kuhn et al., 2019) and served as a pre-existing zone of weakness that controlled the initial slope failure during the first phase of the rock slide. Thus, the decisive role of the pre-existing structural discontinuities for slope stability along the Forkastningsfjellet and the possible reactivation of such inherited zones of weakness is confirmed. This observation has great significance for the stability assessment of the remaining slide blocks of the postglacial Forkastningsfjellet rock slide. They all exhibit pronounced discontinuities systems and weak inhomogeneous bedrock and are bounded by west-dipping block faults (Kuhn et al., 2019). Therefore, the unknown state of activity of the larger sliding blocks and its relevance to hazard assessments make further investigations along the Forkastningsfjellet essential. In this context, several slide blocks have been equipped with bolts and measured by differential global navigation satellite system (dGNSS).

In the regional context, the findings imply that a preliminary assessment of rock slide susceptibility requires a sound knowledge of the geological and structural setting to derive kinematically feasible deformation mechanisms and estimate the potential rock volumes involved.

The origin of the discontinuity system and pre-existing block faults can be attributed mainly to postglacial extensional deformation that was induced by the *huge postglacial Forkastningsfjellet rock slide and its occurrence has been associated with glacial oversteepening* and *debuttressing (*Albertsen, 2016*; Kuhn et al., 2019). The mapped sheeting joints (*Fig. 12A) are also linked to this phase. These non-tectonic extensional joints are attributed to rock stress redistributions and are frequently observed in steep glacially eroded slopes, which lost lateral confinement due to debuttressing (Ballantyne, 2002; Hencher et al., 2011; McColl, 2012). These joints are important pathways for water seepage and serve as releasing surfaces for spalling rock slabs that lead to local steepening of the slope (Fig. 12B).

5.1.2. Rock mass degradation

Strength reduction due to weathering of shale is a well-known phenomenon that is frequently mentioned in shale landslide descriptions. When exposed to weathering processes such as wetting and drying or freezing and thawing cycles, shales are weakened and disintegrate with time (Walkinshaw and Santi, 1996; Stead, 2016). Such a behavior can be observed along the Forkastningsfjellet cliff coast, where weak and degradable shales in different states of transition build a large part of the coastal cliff. Here, the coastal blocks show segments with slaking behavior and soil strength and producing slurrys. In contrast, adjacent segments with higher durability and rock-like strength show translational failures, sheeting joints and spalling (Fig. 12).

In the immediate rock slide area the shale degradation facilitates the gradual retreat of the landslide scarp. This evokes local overhangs and lack of support of the cap rock sandstones leading to topples and rock fall that is characteristic for the current rock slide development.

It is likely that the degradation of the deformed shales in the contact zone of the pre-existing block fault promoted the reactivation and initial movement during the initial slope failure. Also, due to similar geomorphological and geological conditions, we have to take into account that this weakening of the rock mass also affects the stability of the neighboring fault blocks.

5.1.3. Effects of climate warming

Climate change directly influences slope stability in paraglacial environments and might be a preparatory factor and a trigger. Recent warming is thought to influence the periglacial landscape and landslide hazard in the polar and high mountain regions and is therefore intensively studied (e.g., Evans and Clague, 1994; Geertsema et al., 2006; Huggel, 2009; Lewkowicz and Harris, 2005; Allen et al., 2011; Huggel et al., 2012; Gariano and Guzetti, 2016; Panek, 2019; Böhme et al., 2019; Hilger et al., 2021; Etzelmüller et al., 2021).

For periglacial landscapes and particularly for the slopes on Svalbard, the increasing temperatures are correlated with an increasing permafrost degradation and active-layer thickness, leading to active layer detachments and slope instabilities (Harris and Lewkowicz, 1993; Haeberli et al., 2010; Hanssen-Bauer et al., 2019). Changing precipitation trends possibly are associated with increasing freeze-thaw and wetting and drying cycles that might accelerate the disintegration of the shales at Forkastningsfjellet and further weaken the rock mass structure through progressive joint dilation and thawing binding ice. Such mechanical destabilisation of warming bedrock combined with decreasing shear strength of ice-filled rock joints with increasing temperature might be a significant cause for an increasing number of rock slope failures in high mountain areas (Tart, 1996; Davis et al., 2001; Gruber and Haeberli, 2007; Krautblatter et al., 2013; Mamot et al., 2018; Patton et al., 2019). Thawing ice fillings not only reduce the shear strength of the rock mass but also increase the availability of water, which can percolate deeper into the bedrock (e.g. Blikra and Christiansen, 2014; Frauenfelder et al., 2018). This process promotes permafrost degradation through additional advective heat input (Gruber and Haeberli, 2007) and might activate deeper-seated sliding planes.

Though the depth of the permafrost surface is not known for the Forkastningsfjellet coastline, we think that recent warming and melting of ice-filled joints plays an essential role in the general stability of the westerly exposed cliff coast of the Forkastningsfjellet and, in particular, for the triggering of the recent rock slide. This is supported by rock fall

Table 2
Input parameter and value ranges of material- and strength properties used for slope stability assessment using Scoops3D.

Applied properties and search parameter	Value range
Unit weight of rock mass	25 kN/m^3
Cohesion c of pot. Slide plane	0–200 kPa
Friction angle φ of pot. Slide plane	15°- 25°
Lower size limit of pot. Failure volume	1000 m^3
Upper size limit of pot. Failure volume	200,000 m^3

Table 3
Selected results of slope stability calculations with Scoops3D. The trials were performed using the DEM of 2009, a search height interval between 100 and 300 m and Bishop's simplified method. The values of the material properties cohesion, angle of internal friction and the water saturation r_u were varied to approximate a FOS = 1. Calculations with applied water pressure are highlighted in blue, the calculations written in red were used for the comparison between the calculated and the observed slip surface in Fig. 11.

Trial	Cohesion c (kPa)	Friction angle ϕ (°)	Unit weight KN/m³	Water pressure ratio ru	Search Volume (x 1000 m³)	Circle coordinates x,y,z (m)	Circle radius (m)	Affected volume (m³)	FOS
1	150	16	25	0.1	1-175	515010/8694225/100	90,8	155716	1.18
2	150	16	25	0.1	1-200	514970/8694225/135	127	193377	1.11
3	140	16	25	0.1	1-200	514970/8694225/135	127	193377	1.06
4	130	15	25	0.1	1-200	514970/8694225/135	127	193377	0.98
5	**130**	**15**	**25**	**0.1**	**1-175**	**515010/8694225/100**	**90,8**	**155716**	**1.05**
6	140	15	25	0.1	1-175	515010/8694225/100	90,8	155716	1.1
7	130	16	25	0.1	1-200	514970/8694225/135	127	193377	1.01
8	0	30	25	0.1	150-200	515010/8694225/125	108	160183	0.77
9	0	40	25	0.1	150-200	515010/8694225/125	108	160183	1.12
10	**0**	**35**	**25**	**0.1**	**150-200**	**515010/8694225/125**	**108**	**160183**	**0.93**
11	**0**	**37**	**25**	**0.1**	**150-200**	**515010/8694225/125**	**108**	**160183**	**1**
12	150	15	25	-	1-175	515010/8694225/100	91	155716	1.22
13	130	15	25	-	1-175	515010/8694225/120	105	165332	1.11
14	**120**	**15**	**25**	**-**	**1-175**	**515010/8694225/120**	**105**	**165332**	**1.06**
15	110	20	25	-	1-175	514930/8694265/200	206	164838	1.13
16	130	15	25	-	1-200	514970/8694225/135	127	193377	1.05
17	130	15	25	-	100-200	514970/8694185/105	84	160825	1.09
18	150	15	25	-	1-200	514970/8694225/135	127	193377	1.15
19	0	30	25	-	150-200	515010/8694225/125	108	160183	0.9
20	0	35	25	-	150-175	515010/8694225/125	108	160183	1.1
21	**0**	**35**	**25**	**-**	**100-200**	**515010/8694225/125**	**104**	**107126**	**1.05**
22	0	32	25	-	150-200	515010/8694225/125	108	160183	0.98

fragments with ice-filled cracks (Fig. 13) from the toe of the recent rock slide, indicating at least localised melting of ice-filled joints, due to warming of the surficial permafrost. Also, the conducted back-calculation indicated the existence of water pressures during the failure initiation and provided evidence for the role of water percolation.

Therefore, we infer that the decreasing shear strength connected with the weathering (slaking) of the shales along the pre-existing sliding plane combined with a decreasing ice bonding and an increasing water pressure moved the slope from stable to marginally stable conditions.

A two-day rainfall event from August 7th and 8th, 2016, might have been the final triggering event for the failure on August 8th (Fig. 14).

5.2. 2-D Back analysis of recent rock slide

Based on the inferred structural control on the type and extension of the recent rock slide, a back calculation of the slope failure was performed on the basis of a sliding failure along the inherited and reactivated listric surface of failure. To get the necessary information on the geotechnical rock mass properties, several empirical rating schemes like the Rock Mass Rating (RMR) or Slope Mass Rating (SMR) are used (Bieniawski, 1989; Romana, 1985; Moore et al., 2009). Unfortunately, the inaccessibility of the steep terrain and the dangerous rock falls prevented the recording of the rock mass properties with the help of such systems and the measurement of the joint conditions for a kinematic analysis. Therefore, global assumptions of the rock mass properties were employed as a first approximation.

Based on these boundary conditions, the 2-D back analysis was performed using the method of slices. Calculations with varying parameters for cohesion c and friction angle φ yielded reasonable values, both for calculations with and without groundwater influence. We also calculated purely frictional cases with a cohesion c = 0 kPa, but these results were discarded as they revealed unrealistic values for the friction angle along the surface of rupture during failure. We selected the cohesion/friction angle value pair of 130 kPa/15° for dry conditions and the cohesion/ friction angle value pairs of 175 kPa/15° and 150 kPa/20° with water pressure as the most appropriate shear strength properties of basal sliding plane at failure. These values are comparable to published examples in the literature (e.g. Wyllie and Mah, 2004; Glastonbury and Fell, 2010), but should be validated by laboratory testing on rock samples. Such robust and reliable geotechnical data are necessary to evaluate future observed rock slope deformations and to perform regional susceptibility analyses. Given the observations of wet slopes, localised seepage along joint surfaces and ice-filled rock fall fragments (Fig. 14) during the summer field trips, we infer that the calculations with water pressure most realistically reflect the conditions at failure in the summer of 2016. In contrast, the calculations without water pressure might reflect winter conditions, during which the coastal area is completely frozen. The observations and calculation results imply that the continued warming trend and the correlated permafrost thaw might alter the general landslide regime at Forkastningsfjellet. The loss of bedrock shear strength due to ice loss will lead to higher pore water pressures in summer times. In combination with a progressive rock mass weakening due to increasing freeze-thaw processes, an increase of the future rock slide activity at Forkastningsfjellet is likely (Gischig et al., 2011; Draebing et al., 2017).

5.3. 3-D Back analysis of recent rock slide with Scoops3D

The 3-D back analysis with Scoops3D was performed using the same boundary conditions and input variables as in the 2-D approach. Given the known extension of the initial failure surface, the calculated slip

surfaces were visually compared, and the respective sets of the associated shear strength properties deduced.

Again, calculations with cohesion c = 0 required unrealistic high friction angles >35° (without water pressure) and > 37° (with ru = 0.1) to achieve a FOS of 1. Applying a likely range of friction angle and cohesion c, the best match was found with the value pairs 130 kPa/15° with water pressure (ru = 0.1) and 120 kPa/15° for calculations without water pressure. However, the latter revealed a smaller affected rock volume.

In this context, it has to be stressed that the analysis with Scoops3D calculates the slope stability for a rock mass with defined rock mass properties and does not take into account any zones of weakness or sliding surfaces that could be reactivated. In addition, the calculations showed that the results are sensitive to the 'maximum search volume' boundary condition. Thus, although increasing the maximum search volume from 175 k to 200 k resulted in a realistic range of affected rock volume for all calculations (field estimate 175,000 m^3), the search with a maximum search volume of 200 k generated too large and dislocated slip surfaces, which were not congruent with the real shear area.

Nevertheless, the results show that Scoops3D is a valuable tool to investigate the current state, possible trigger scenarios and the potentially affected volume of rock slope failures along the Forkastningsfjellet coastline, as the morphostructural and geological model is well established.

The derived properties of the sliding plane are a first approximation for the strength of block bounding slide planes of Forkastningsfjellet. As in the 2-D analysis, this dataset needs to be verified by shear strength investigations on respective rock samples in the laboratory, so that it could be used for stability analysis of the remaining rock slide blocks along the coastline of Forkastningsfjellet as well as on other rock slopes of the Isfjorden coast that are currently being investigated.

6. Conclusions

Based on a thorough morphostructural analysis of a cliff coast segment of Forkastningsfjellet, a back analysis of a recent rock slide was carried out. Using a conventional 2-D and a 3-D approach with the Scoops3D application, the controlling and triggering factors of the cliff failure were studied. Slope failure was initiated along a pre-existing listric block fault that was inherited from the postglacial Forkastningsfjellet rock slide event (Kuhn et al., 2019).

The cause of the initial failure is attributed to a shear strength decrease along the pre-existing sliding plane, possibly in combination with a degradation of the affected weak shales of the Rurikfjellet Formation, which build up the lowest two-thirds of the steep to oversteepened slope. In addition, weather and climate-related causes are thought to influence slope stability, as increasing temperatures and permafrost degradation reduce bonding forces in the thawing fractures (Davis et al., 2001; Mamot et al., 2018) and increase freeze-thaw cycles that weaken the slaking shales. The final trigger of the rock side is assigned to increased water pressures on the sliding plane, possibly enhanced by a two-day rainfall event.

For an improved understanding of governing processes of coastal cliff instabilities along the Isfjorden, more field work and much more information from different multidisciplinary investigations and technologies is necessary (e.g. Etzelmüller et al., 2021; Hilger et al., 2021; Krautblatter et al., 2013; Böhme et al., 2013). The results obtained so far justify a more detailed investigation of the reactivation potential of large slide blocks along the Forkastningsfjellet coastline.

Given the predicted climate warming of the region, field surveys should be intensified to identify metastable slopes and install long-term monitoring equipment to assess potential movements and support hazard assessments.

This task could be supported by the Scoops3D software. The application of this tool showed that it is capable of predicting the locations and affected volumes of landslides with reasonable accuracy, when the geological and structural setting is well established. Under the premises of such reliable input data and necessary experimental laboratory data, Scoops3D can be used for studies on the occurrence of future landslides in study areas with comparable geological and morphostructural settings. It also might be used as a quick screening tool to identify metastable areas within the landscape that may warrant subsequent more detailed stability analysis.

Investigation of climate-controlled factors should be intensified to understand better permafrost degradation and, more specifically, the temperature development in coastal slopes. It is evident that the depth of the permafrost is an important controlling factor that defines the position of the sliding surface and the water content of the rock mass.

Declaration of competing interest

The authors declare that they have no known competing financial interests or personal relationships that could have appeared to influence the work reported in this paper.

Acknowledgements

This paper results from fieldwork carried out in summer 2017 and 2019. The authors wish to thank BGR and NGU for funding the fieldwork. Chr. Kasch supported the fieldwork with valuable information and equipment. Terrapolaris and Hennigsen Transport and Guiding along with affiliated wildlife guards are thanked for supporting the field campaigns.

The authors also wish to acknowledge the reviews and helpful comments of S. McColl and an unknown referee.

References

Albertsen, A., 2016. Cenozoic compressional tectonics and post-glacial landsliding at Forkastningsfjellet, Spitsbergen, Svalbard. MS Thesis. Department of Geosciences Faculty of Mathematics and Natural Sciences, University of Oslo, Norway.

Allen, K.A., Cox, S.C., Owens, I.F., 2011. Rock avalanches and other landslides in the central Southern Alps of New Zealand: a regional study considering possible climate change impacts. Landslides 8, 33–48.

Ballantyne, C.K., 2002. Paraglacial geomorphology. Quat. Sci. Rev. 21, 1935–2017.

Ballantyne, C.K., Stone, J.O., 2013. Timing and periodicity of paraglacial rock-slope failures in the Scottish Highlands. Geomorphology 186, 150–161.

Bergh, S.G., Braathen, A., Andresen, A., 1997. Interaction of basement-involved and thin-skinned tectonism in the Tertiary fold thrust belt of central Spitsbergen, Svalbard. Am. Ass. Petrol. Geol. Bull. 81, 637–661.

Bessette-Kirton, E.K., Coe, J.A., 2020. A 36-year record of rock avalanches in the Saint Elias Mountains of Alaska, with implications for future hazards. Front. Earth Sci. 8 (293). https://doi.org/10.3389/feart.2020.00293.

Bieniawski, Z.T., 1989. Engineering Rock Mass Classification: A Complete Manual for Engineers and Geologists Inmining, Civil, and Petroleum Engineering. JWiley.

Bishop, A.W., 1955. The use of the slip circle in the stability analysis of earth slopes. Geotechnique 5, 7–17.

Bishop, A.W., Morgenstern, N., 1960. Stability coefficients for earth slopes. Geotechnique 10, 164–169.

Blikra, L.H., Christiansen, H.H., 2014. A field-based model of permafrost-controlled rock slide deformation in northern Norway. Geomorphology 208, 34–39.

Bohloli, B., Skurtveit, E., Grande, L., Titlestad, G.O., Borresen, M.H., Johnsen, O., Braathen, A., 2014. Evaluation of reservoir and cap-rock integrity for the Longyearbyen CO2 storage pilot based on laboratory experiments and injection tests. Nor. J. Geol. 94, 171–187.

Bohloli, B., Skurtveit, E., Choi, J., Grande, L., Soldal, M., Wilkinson, H.D., 2015. Direct Shear Tests on Cretaceous Shales from Cap-Rock of the Longyearbyen CO2 Storage Pilot, Svalbard, Norway. Second EAGE Workshop on Geomechanics and Energy, Celle, Germany.

Böhme, M., Saintot, A., Henderson, I.H.C., Henriksen, H., Hermanns, R.L., 2011. Rock slope instabilities in Sogn and Fjordane County, Norway: a detailed structural and geomorphological analysis. Geol. Soc. Lond., Spec. Publ. 351, 97–111.

Böhme, M., Hermanns, R.L., Oppikofer, T., Fischer, L., Bunkholt, H.S., Eiken, T., Pedrazzini, A., Derron, M.-H., Jaboyedoff, M., Blikra, L.H., 2013. Analyzing complex rock slope deformation at Stampa, western Norway, by integrating geomorphology, kinematics and numerical modelling. Eng. Geol. 154, 116–130.

Böhme, M., Hermanns, R., Gosse, J., Hilger, P., Eiken, T., Lauknes, T., Dehls, J., 2019. Comparison of monitoring data with paleo–slip rates: cosmogenic nuclide dating detects acceleration of a rockslide. Geology 47, 339–342.

Borgatti, L., Soldati, M., 2010. Landslides as a geomorphological proxy for climate change: a record from the Dolomites (northern Italy). Geomorphology 120, 56–64.

Christiansen, H.H., Etzelmüller, B., Isaksen, K., Juliussen, H., Farbrot, H., Humlum, O., Johansson, M., Ingeman-Nielsen, T., Kristensen, L., Hjort, J., Holmlund, P., Sannel, A.B.K., Sigsgaard, C., Akerman, H.J., Foged, N., Blikra, L.H., Pernosky, M.A., Ødegard, R.S., 2010. The thermal state of permafrost in the nordic area during the international polar year 2007–2009. Permafr. Periglac. Process. 21, 156–181.

Crozier, M.J., 1999. Prediction of rainfall-triggered landslides: a test of the antecedent water status model: Earth Surf. Process. Landf. 24, 825–833.

Crozier, M.J., 2010. Deciphering the effect of climate change on landslide activity: a review. Geomorphology 124, 260–267.

Cruden, D.M., Varnes, D.J., 1996. Landslides. Types and Processes. In: Turner, A.K., Schuster, R.L. (Eds.), Landslides. Investigation and Mitigation. Transport Research Board, National Research Council, Washington D. C Special Report 247.

Dallmann, W.K., Kjaernet, T., Nottvedt, A., 2001. Geological Map of Svalbard 1:100,000, Sheet C9G Adventdalen. Norsk Polarinstitutt.

Davis, M.C.R., Hamza, O., Harris, C., 2001. The effect of rise in mean annual temperatures on the stability of rock slopes containing ice-filled discontinuities. Permafr. Periglac. Process. 12, 137–144.

Dikau, R., Brundsen, D., Schrott, L., Ibsen, M., 1996. Landslide Recognition. Wiley.

DJI Terra, 2021. https://www.dji.com/de/dji-terra (accessed 04 February 2021).

Draebing, D., Krautblatter, M., Hoffmann, T., 2017. Thermo-cryogenic controls of fracture kinematics in permafrost rockwalls. Geophys. Res. Lett. 44, 3535–3544.

Duncan, J.M., 1996. Soil Slope Stability Analysis. In: Turner, A.K., Schuster, R.L. (Eds.), Landslides: Investigation and Mitigation, Transportation Research Board National Research Council. Special Report 247. National Academy Press, Washington D.C., USA.

Duncan, J.M., Wright, S.G., Brandon, T.L., 2014. Soil Strength and Slope Stability. John Wiley and Sons.

Dypvik, H., Nagy, J., Eikeland, T.A., Backer, O.K., Johansen, H., 1991. The depositional conditions of the Bathonian to Hauterivian Janusfjellet Subgroup. Spitsbergen; a revised lithostratigraphy. Sediment. Geol. 72, 55–78.

Eberhardt, E., Stead, D., Coggan, J.S., 2004. Numerical analysis of initiation and progressive failure in natural rock slopes e the 1991 Randa rockslide. Int. J. Rock Mech. Min. 41, 69–87.

Etzelmüller, B., Czedirda, J., Magnin, F., Duvillard, P.A., Malet, E., Ravanel, L., Aspaas, A., Kristensen, L., Skrede, I., Majala, G.D., Jacobs, B., Leinauer, J., Hauck, C., Hilbich, C., Böhme, M., Hermanns, R., Eriksen, H.Ø., Krautblatter, M., Westermann, S., 2021. Permafrost in monitored unstable rock slopes in Norway – new insights from rock wall temperature monitoring, geophysical surveying and numerical modelling. Earth Surf. Dynam. Discuss. 2021, 1–55.

Evans, S.G., Clague, J.J., 1994. Recent climatic change and catastrophic geomorphic processes in mountain environments. Geomorphology 10, 107–128.

Fischer, L., Purves, R.S., Huggel, C., Noetzli, J., Haeberli, W., 2012. On the influence of topographic, geological and cryospheric factors on rock avalanches and rockfalls in high-mountain areas. Nat. Hazards Earth Syst. Sci. 12, 241–254.

Førland, E.J., Benestad, R.E., Hanssen-Bauer, I., Haugen, J.E., Skaugen, T.E., 2011. Temperature and Precipitation Development at Svalbard 1900–2100. Adv. Meteorol. 2011, 1–14. https://doi.org/10.1155/2011/893790.

Frauenfelder, R., Isaksen, K., Nötzli, J., Lato, M.J., 2018. Ground thermal and geomechanical conditions in a permafrost-affected high-latitude rockslide site (Polvartinden, Northern Norway). Cryosphere 12, 1531–1550.

Gariano, S.L., Guzetti, F., 2016. Landslides in a changing climate. Earth Sci. Rev. 162, 227–252.

Gauthier, D., Anderson, S.A., Fritz, H.M., Giachetti, T., 2018. Karrat Fjord (Greenland) tsunamigenic landslide of 17 June 2017: initial 3D observations. Landslides 15, 327–332. https://doi.org/10.1007/s10346-017-0926-4.

Geertsema, M., Clague, J.J., Schwab, J.W., Evans, S.G., 2006. An overview of recent large catastrophic landslides in northern British Columbia, Canada. Eng. Geol. 83, 120–143.

Gilbert, G.L., Instanes, A., Sinitsyn, A.O., Aalberg, A., 2019. Characterization of two sites for geotechnical testing in permafrost: Longyearbyen, Svalbard. AIMS Geosciences 5, 868–885. https://doi.org/10.3934/geosci.2019.4.868.

Gischig, V.S., Moore, J.R., Evans, K.F., Amann, F., Loew, S., 2011. Thermomechanical forcing of deep rock slope deformation: 1. Conceptual study of a simplified slope. J. Geophys. Res. Earth Surf. 116 (F4).

Gjelberg, J., Steel, R., 1995. Helvetiafjellet Formation (Barremian-Aptian), Spitsbergen: characteristics of a transgressive succession. In: Steel, R., Felt, V.L., Johannesen, E.P., Mathieu, C. (Eds.), Sequence Stratigraphy on the Northwest European Margin. vol. 5. Norwegian Petroleum Society Special Publication, pp. 571–573.

Glade, T., Crozier, M., 2005. The nature of landslide hazard impact. In: Glade, T., Anderson, M., Crozier, M. (Eds.), Landslide hazard and risk. John Wiley and Sons Ltd, Chichester.

Glastonbury, J., Fell, R., 2010. Geotechnical characteristics of large rapid rock slides. Can. Geotech. J. 47, 116–132.

Griffiths, J., Whitworth, M., 2012. Engineering geomorphology of landslides. In: Clague, J., Stead, D. (Eds.), Landslides: Types, Mechanisms and Modeling. Cambridge University Press, Cambridge, pp. 172–186. https://doi.org/10.1017/CBO9780511740367.016.

Gruber, S., Haeberli, W., 2007. Permafrost in steep bedrock slopes and its temperature-related destabilization following climate change. J. Geophys. Res. 112, 1–10 F02S18.

Haeberli, W., Noetzli, J., Arenson, L., Delaloye, R., Gärtner-Roer, I., Gruber, S., Isaksen, K., Kneisel, C., Krautblatter, M., Phillips, M., 2010. Mountain permafrost: development and challenges of a young research field. J. Glaciol. 56, 1043–1058.

Hanssen-Bauer, I., Førland, E., Hisdal, H., Mayer, S., Sandø, A., Sorteberg, A. (Eds.), 2019. Climate in Svalbard 2100 - a knowledge base for climate adaptation. NCCS report No 1/2019, pp. 207.

Harris, C., Lewkowicz, A.G., 1993. Form and internal structure of active-layer detachment slides, Fosheim Peninsula, Ellesmere Island, N.W.T., Canada. Can. J. Earth Sci. 30, 1708–1714.

Harris, C., Kern-Luetschg, M., Christiansen, H.H., Smith, F., 2011. The role of interannual climate variability in controlling solifluction processes, Endalen, Svalbard. Permafr. Periglac. Process. 22, 239–253. https://doi.org/10.1002/ppp.727.

Hartvich, F., Blahut, J., Stemberk, J., 2017. Rock avalanche and rock glacier: a compound landform study from Hornsund, Svalbard. Geomorphology 276, 244–256.

Hencher, S., Lee, S., Carter, T., Richards, L., 2011. Sheeting joints: characterisation, shear strength and engineering. Rock Mech. Rock. Eng. 44, 1–22.

Henderson, I., Saintot, A., 2011. Regional spatial variations in rockslide distribution from structural geology ranking: an example from Storfjorden, western Norway. Geol. Soc. Lond. Spec. Publ. 351, 79–95.

Hermanns, R.L., Longva, O., 2012. Rapid rock-slope failures. In: Clague, J.J., Stead, D. (Eds.), Landslides: Types, Mechanisms and Modeling. Cambridge University Press, pp. 59–70. https://doi.org/10.1017/CBO9780511740367.007.

Hermanns, R., Niedermann, S., Villanueva Garcia, A., Schellenberger, A., 2006. Rock avalanching in the NW argentine Andes as a result of complex interactions of lithologic, structural and topographic boundary conditions, climate change and active tectonics. In: Evans, S.G., Mugnozza, G.S., Strom, A., Hermanns, R.L. (Eds.), Landslides from Massive Rock Slope Failure. NATO Science Series. vol. 49. Springer, Dordrecht, pp. 539–569. https://doi.org/10.1007/978-1-4020-4037-5_27.

Hermanns, R.L., L'Heureux, J.S., Blikra, L.H., 2013. Landslide triggered tsunami, displacement wave. In: Bobrowsky, P.T. (Ed.), Encyclopedia of Natural Hazards. Encyclopedia of Earth Sciences Series. Springer, Dordrecht. https://doi.org/10.1007/978-1-4020-4399-4_95.

Higman, B., Shugar, D.H., Stark, C.P., Ekström, G., Koppes, M.N., Lynett, P., Dufresne, A., Haeussler, P.J., Geertsema, M., Gulick, S., 2018. The 2015 landslide and tsunami in Taan Fiord, Alaska. Sci. Rep. 8, 12993. https://doi.org/10.1038/s41598-018-30475-w.

Hilger, P., Hermanns, R.L., Czekirda, J., Myhra, K.S., Gosse, J.C., Etzelmüller, B., 2021. Permafrost as a first order control on long-term rock-slope deformation in (Sub-)Arctic Norway. Quat. Sci. Rev. 251, 106718.

Hoek, E., Bray, J., 1981. Rock Slope Engineering. 3rd ed. Institution of Mining and Metallurgy, London.

Hoek, E., Brown, E.T., 1997. Practical estimates of rock mass strength. Int. J. Rock Mech. Min. Sci. 34, 1165–1186.

Hutchinson, J.N., 1988. General report: morphological and geotechnical parameters of landslides in relation to geology and hydrogeology. In: Bonnard, C. (Ed.), Proc., Fifth International Symposium on Landslides. 1. A.A. Balkema, Rotterdam, Netherlands, pp. 3–35.

Huggel, C., 2009. Recent extreme slope failures in glacial environments: effects of thermal perturbation. Quat. Sci. Rev. 28, 1119–1130.

Huggel, C., Clague, J., Korup, O., 2012. Is climate change responsible for changing landslide activity in high mountains? Earth Surf. Process. Landf. 37, 77–91.

Humlum, O., Instanes, A., Sollid, J.L., 2003. Permafrost in Svalbard: a review of research history, climatic background and engineering challenges. Polar Res. 22, 191–215.

Hungr, O., Leroueil, S., Picarelli, L., 2014. The Varnes classification on landslide types, an update. Landslides 11, 167–194.

Isaksen, K., Sollid, J.L., Holmlund, P., Harris, C., 2007. Recent warming of mountain permafrost in Svalbard and Scandinavia. J. Geophys. Res. 112, F02S04. https://doi.org/10.1029/2006JF000522.

Jaboyedoff, M., Couture, R., Locat, P., 2009. Structural analysis of Turtle Mountain (Alberta) using digital elevation model: toward a progressive failure. Geomorphology 103, 5–16. https://doi.org/10.1016/j.geomorph.2008.04.012.

Korup, O., Clague, J.J., 2009. Natural hazards, extreme events, and mountain topography. Quat. Sci. Rev. 28, 977–990.

Krautblatter, M., Funk, D., Günzel, F.K., 2013. Why permafrost rocks become unstable: a rock–ice-mechanical model in time and space. Earth Surf. Process. Landf. 38, 876–887.

Kuhn, D., Redfield, T.F., Hermanns, R.L., Fuchs, M., Torizin, J., Balzer, D., 2019. Anatomy of a mega-rock slide at Forkastningsfjellet, Spitsbergen and its implications for landslide hazard and risk considerations. Nor. J. Geol. 99, 41–61.

Kuhn, D., Hermanns, R.L., Torizin, J., Fuchs, M., Redfield, T., Eilertsen, R., Balzer, D., 2021. Forkastningsfjellet Rock Slide, Spitsbergen: state of activity in a changing climate. In: Vilímek, V., Wang, F., Strom, A., Sassa, K., Bobrowsky, P.T., Takara, K. (Eds.), Understanding and Reducing Landslide Disaster Risk. WLF 2020. ICL Contribution to Landslide Disaster Risk Reduction. Springer, Cham.

Lewkowicz, A.G., Harris, C., 2005. Morphology and geotechnique of active-layer detachment failures in discontinuous and continuous permafrost, northern Canada. Geomorphology 69, 275–297.

Major, H., Nagy, J., 1972. Geology of the Adventdalen map area. Skrifter 138. Norsk Polarinstitutt.

Mamot, P., Weber, S., Schröder, T., Krautblatter, M., 2018. A temperature-and stress-controlled failure criterion for ice-filled permafrost rock joints. Cryosphere 12, 3333–3353. https://doi.org/10.5194/tc-12-3333-2018.

McColl, S.T., 2012. Paraglacial rock-slope stability. Geomorphology 153, 1–16.

McColl, S.T., Draebing, D., 2019. Rock slope instability in the proglacial zone: state of the art. In: Heckmann, T., Morche, D. (Eds.), Geomorphology of Proglacial Systems, Landform and Sediment Dynamics in Recently Deglaciated Alpine Landscapes, pp. 119–141.

Landslides and climate change: challenges and solutions. In: McInnes, R., Jakeways, J., Fairbank, H., Mathie, E. (Eds.), Proceedings of the International Conference on Landslides and Climate Change. Taylor & Francis, Ventnor. https://doi.org/10.1201/noe0415443180.

Midtkandal, I., Nystuen, J.P., Nagy, J., Mørk, A., 2008. Lower Cretaceous lithostratigraphy across a regional subaerial unconformity in Spitsbergen: the Rurikfjellet and Helvetiafjellet formations. Nor. J. Geol. 88, 287–304.

Moore, J.R., Sanders, J.W., Dietrich, W.E., Glaser, S.D., 2009. Influence of rock mass strength on the erosion rate of Alpine Cliffs. Earth Surf. Process. Landf. 34, 1339–1352.

Nordli, Ø., Przybylak, R., Ogilvie, A.E.J., Isaksen, K., 2014. Long-term temperature trends and variability on Spitsbergen: the extended Svalbard Airport temperature series, 1898–2012. Polar Res. 33, 1–23.

Norsk Polarinstitutt (2018) Geological maps of Svalbard. https://svalbardkartet.npolar.no/html5/index.html?viewer=svalbardkartet.html5 (accessed 04 February 2021).

Panek, T., 2019. Landslides and Quaternary climate changes-the state of the art. Earth Sci. Rev. https://doi.org/10.1016/j.earscirev.2019.05.015.

Parker, J.R., 1967. The Jurassic and Cretaceous sequence in Spitsbergen. Geol. Mag. 104, 487–505.

Patton, A.I., Rathburn, S.L., Capps, D.M., 2019. Landslide response to climate change in permafrost regions. Geomorphology 340, 116–128.

Petley, D., 2012. Global patterns of loss of life from landslides. Geology 40, 927–930. https://doi.org/10.1130/G33217.1.

Reid, M.E., Christian, S.B., Brien, D.L., 2000. Gravitational stability of three-dimensional stratovolcano edifices. J. Geophys. Res. 105, 6043–6056.

Reid, M.E., Christian, S.B., Brien, D.L., Henderson, S.T., 2015. Scoops3D—Software to analyze 3D slope stability throughout a digital landscape. U.S. Geological Survey Techniques and Methods. https://doi.org/10.3133/tm14A1. book 14, chap. A1, 218 p.

Romana, M., 1985. New Adjustment Ratings for Application of Bieniawski Classification to Slopes. International Symposium on the Role of Rock Mechanics, Zacatecas, ISRM, pp. 49–53.

Røsvik, H.K., 2016. Stort fjellmassiv har rast ut. http://svalbardposten.no/natur-og-miljo/nyheter/stort-fjellmassiv-rast-ut/19.7473.

Saintot, A., Henderson, I.H.C., Derron, M.-H., 2011. Inheritance of ductile and brittle structures in the development of large rock slope instabilities: examples from western Norway. In: Jaboyedoff, M. (Ed.), Slope Tectonics. Geol. Soc. London, Spec. Publ.. vol. 351, pp. 27–78

Stead, D., 2016. The influence of shales on slope instability. Rock Mech. Rock. Eng. 49, 635–651.

Stead, D., Wolter, A., 2015. A critical review of rock slope failure mechanisms: the importance of structural geology. J. Struct. Geol. 74, 1–23.

Svennevig, K., Dahl-Jensen, T., Keiding, M., Merryman Boncori, J.P., Larsen, T.B., Salehi, S., Munck Solgaard, A., Voss, P.H., 2020. Evolution of events before and after the 17 June 2017 rock avalanche at Karrat Fjord, West Greenland – a multidisciplinary approach to detecting and locating unstable rock slopes in a remote Arctic area. Earth Surf. Dynam. 8, 1021–1038.

Tart, R.G., 1996. Permafrost. In: Turner, A.K., Schuster, R.L. (Eds.), Landslides: Investigation and Mitigation, Transportation Research Board National Research Council. Special Report 247. National Academy Press, Washington D.C., USA.

Tessensohn, F., Piepjohn, K., 2000. Eocene compressive deformation in Arctic Canada and Svalbard and its plate tectonic causes. In: Roland, N.W., Tessensohn, F. (Eds.), ICAM III—III. In: International Cconference on arctic margins I, Polarforschung. vol. 68, pp. 121–124.

Varnes, D.J., 1978. Slope movement types and processes. In: Schuster, R.L., Krizek, R.J. (Eds.), Landslide Analysis and Control, Special Report 176. Transportation Research Board, National Academy of Sciences, Washington DC, pp. 12–33.

Vick, L.M., Böhme, M., Rouyet, L., Bergh, S.G., Corner, G.D., Lauknes, T.R., 2020. Structurally controlled rock slope deformation in northern Norway. Landslides 17, 1745–1776. https://doi.org/10.1007/s10346-020-01421-7.

Walkinshaw, J.L., Santi, P.M., 1996. Shales and other degradable materials. In: Turner, A.K., Schuster, R.L. (Eds.), Landslides: Investigation and Mitigation, Transportation Research Board National Research Council. Special Report 247. National Academy Press, Washington D.C., USA.

Whalley, W.B., 1974. The mechanics of high-magnitude, low-frequency rock failure, and its importance in a mountainous area. Geographical Papers 27. Department of Geography, University of Reading (48 pp).

Wieczorek, G.F., 1996. Landslide triggering mechanism. In: Turner, A.K., Schuster, R.L. (Eds.), Landslides: Investigation and Mitigation, Transportation Research Board National Research Council. Special Report 247. National Academy Press, Washington D.C., USA.

Wyllie, D.C., Mah, C.W., 2004. Rock Slope Engineering: Civil and Mining. 4th edition. Taylor and Francis.